Supplementary Material

Quasi-flatband resonances and bound states in the continuum in coupled photonic topological defects for boosting light-matter interactions

Xinpeng Jiang(姜鑫鹏),[1,#] Mingyu Luo(罗鸣宇) ,[2,#] Zhaojian Zhang(张兆健),[1,*] Jian Wei You(游检卫),[3] Zhihao Lan(兰智豪),[4] and Junbo Yang(杨俊波),[1,]**

[1]Department of Physics, National University of Defense Technology, Changsha 410073, China

[2]Photonics Research Institute, Department of Electrical and Electronic Engineering, The Hong Kong Polytechnic University, Kowloon, Hong Kong 999077, China

[3]State Key Laboratory of Millimeter Waves, School of Information Science and Engineering, Southeast University, Nanjing, 210096, China

[4]Department of Electronic and Electrical Engineering, University College London, London WC1E 7JE, United Kingdom

#These authors contributed equally

*Corresponding author: zhangzhaojian@nudt.edu.cn; **corresponding author: yangjunbo@nudt.edu.cn

1. Band structure and Q-factor analysis for different *m* values

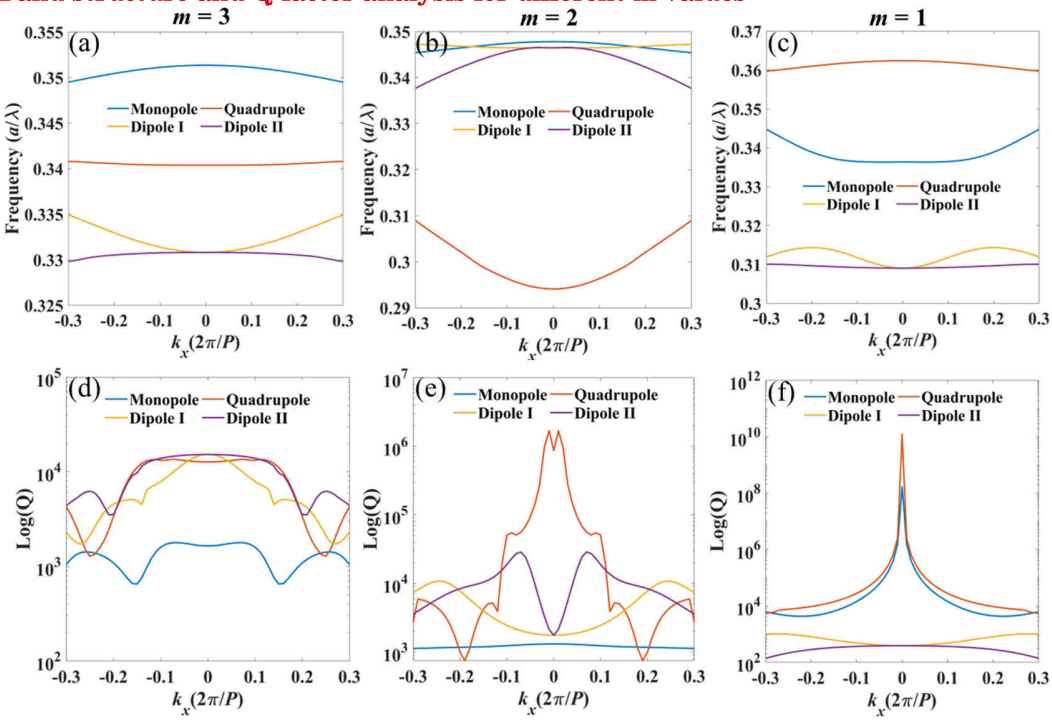

Fig. S1 (a-c) band structures of topological corner (defect) modes for different values of *m*. (d-f) Q factors of topological corner (defect) modes for different values of *m*.

Fig. S1(a–c) and S1(d–f) present the band structures and corresponding Q factors of topological corner (defect) modes for different values of *m*, respectively. As shown in Fig. S1(a), when *m* = 3, the quadrupole band appears relatively flat, while the other bands remain dispersive. This flatband arises from weak internal coupling among the optical fields at the four corners and uniform coupling to adjacent sites, consistent with

quadrupole symmetry. In Fig. S1(d), no BIC is observed due to the presence of multiple diffraction-induced radiative channels. Compared to the m = 1 case, the flatband quadrupole corner mode at m = 3 exhibits a lower local field intensity owing to its sparse spatial distribution, and diminished field enhancement in the absence of BICs, resulting in weaker light–matter interaction. At m = 2, the coupling between corner fields becomes stronger, giving rise to four dispersive bands as illustrated in Fig. S1(b), along with a reordering of the eigenfrequencies of the corner modes. However, because the supercell period remains larger than the subwavelength scale, BICs still do not form, as seen in Fig. S1(e). Notably, for m = 1, the corner modes transform into defect modes, simultaneously exhibiting flatband and BIC characteristics, as shown in Figs. S1(c) and S1(f).

2. Detailed form of the TB approximation

In a square lattice, the TB approximation can be expressed in the following form:

$$\omega(\mathbf{k})-\omega_0=-2t_1\left[\cos(k_x a)+\cos(k_y a)\right]-4t_2\cos(k_x a)\cos(k_y a) \\ -2t_3\left[\cos(2k_x a)+\cos(2k_y a)\right] \quad (1)$$

where t_1, t_2, and t_3 represent the coupling coefficients for nearest neighbor (NN, first-nearest-neighbor), next-nearest neighbor (NNN, second-nearest-neighbor), and next-next-nearest neighbor (3NN, third-nearest-neighbor) interactions, respectively. Fig. S2 illustrates the analytically fitted band structures obtained using the TB model with varying coupling ranges. The results show that considering only up to NNN coupling is insufficient to accurately reproduce the full band structure, particularly the features associated with the monopole and dipole I bands. A satisfactory agreement between the TB model and numerical simulations is achieved only when the 3NN coupling terms are included, as demonstrated in Fig. S2(c).

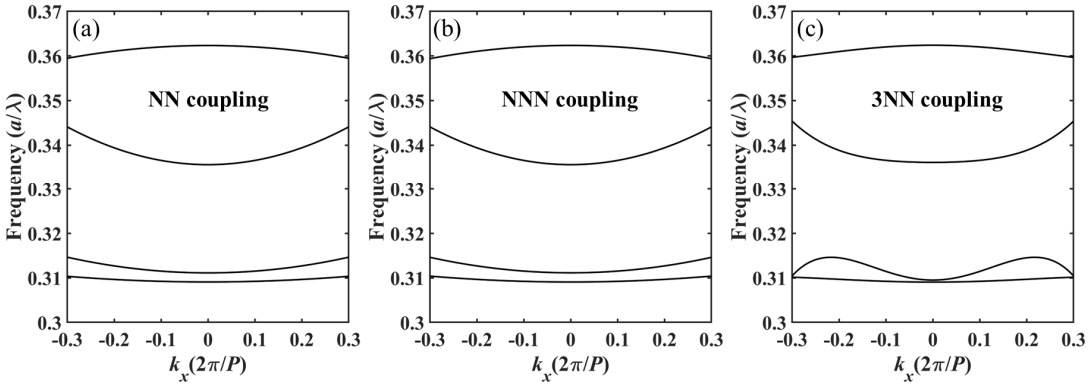

Fig. S2 (a-c) the analytically fitted band structures obtained using the TB model with varying coupling ranges.

3. Multipole analysis for topological defect modes

To gain deeper insight into the origin of these defect modes, we calculate their scattering powers at the Γ point for various multipoles in the Cartesian coordinate system using multipole scattering theory [1]. Fig. S3(a) presents the scattering power distribution for different multipoles associated with the four defect modes. Specifically, the qBIC is predominantly characterized by an electric quadrupole (EQ) moment, as confirmed by analyzing its in-plane x- or y-components of the electric fields, which reveal a higher-order spatial charge distribution, as shown in Fig. S3 (b). According to the theory of the multipolar origin of BICs [2], the directivity pattern of this in-plane EQ moment suppresses radiation along the vertical z-axis, as illustrated in the inset of Fig. S3(a). Radiation in other directions is prohibited by the sub-diffraction regime of the supercell,

leading to the formation of the qBIC. The mBIC is predominantly associated with contributions from the magnetic dipole (MD) and magnetic quadrupole (MQ) moments. The MD moment originates from strong in-phase MDs, as evidenced by the z-component of the magnetic field and the in-plane looped displacement current flows, depicted in Fig. S3(c). These checkerboard arrays of alternating-phase MDs also collectively give rise to an MQ moment. Both the out-of-plane MD and MQ moments suppress radiation along the z-axis, as shown in the inset of Fig. S3(a), resulting in the formation of the mBIC. In contrast, the Res I and II exhibit richer multipolar characteristics, with significant contributions from the toroidal dipole (TD), MQ, and electric dipole (ED) moments. For instance, dRes II is characterized by a pair of out-of-plane MDs with opposite phases, inducing in-plane current flows in opposite circulatory directions, as shown in Fig. S3(d). These current flows form a closed out-of-plane magnetic vortex, indicative of a TD moment, illustrated in Fig. S3(e). The in-plane TD moment, in combination with the in-plane ED moment, supports radiation along the z-axis as indicated in the inset of Fig. S3(a), resulting in the leaky nature of these modes at the Γ point. These findings further highlight the rich multipole landscape of topological defect modes in PhC slabs.

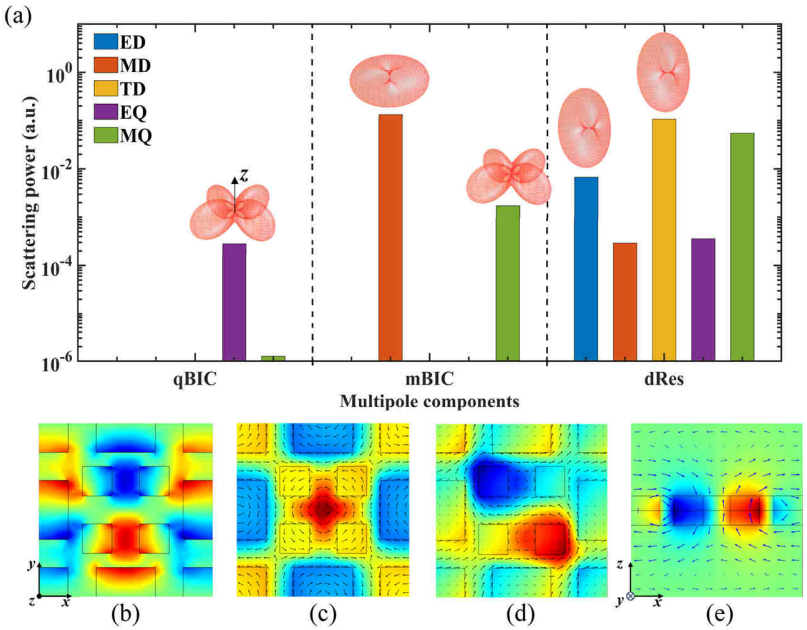

Fig. S3 (a) Scattering power distributions at the Γ point for the four defect modes, decomposed into various multipole contributions in the Cartesian coordinate system. Insets depict the radiation patterns of the corresponding multipoles. (b) E_y field distributions for the qBIC. (c) H_z field distributions and in-plane current flows (black arrows) for the mBIC. (d) Hz field distributions and in-plane current flows (black arrows) for the dRes II. (e) H_z field distributions and out-of-plane magnetic flux (blue arrows) for the dRes II.

4. Topological charges of the two BICs

We extend our investigation into the properties of the two BICs by examining their far-field radiation characteristics in momentum space. Fig. S4(a) and 4(b) present the polarization maps of the qBIC and mBIC, respectively. In the far field, vortex centers are prominently observed in the polarization field, indicating regions where the polarization direction is undefined. This observation confirms that the two BICs are decoupled from the radiation continuum at the Γ point, leading to a theoretically infinite Q-factor. The two BICs exhibit distinct configurations in their polarization maps, which can be characterized by an integer topological charge defined as follows [3]:

$$q = \frac{1}{2\pi} \oint_C d\mathbf{k} \cdot \nabla_{\mathbf{k}} \phi(\mathbf{k}) \qquad (2)$$

where $\phi(\mathbf{k})$ represents the angle between the polarization major axis and the x-axis, and C denotes a simple closed path in momentum space encircling the BIC in a counterclockwise direction. Fig. S4(c) and (d) illustrate the simulated azimuthal angle maps of polarizations for the two BIC bands, revealing different features. For the qBICs, the total winding angle along any counterclockwise loop around the central singularity is 4π, corresponding to a topological charge of $q = +2$. In contrast, for the mBICs, the total winding angle is −4π, yielding a topological charge of $q = -2$. These results provide a clear demonstration of the distinct topological characteristics of the two BICs.

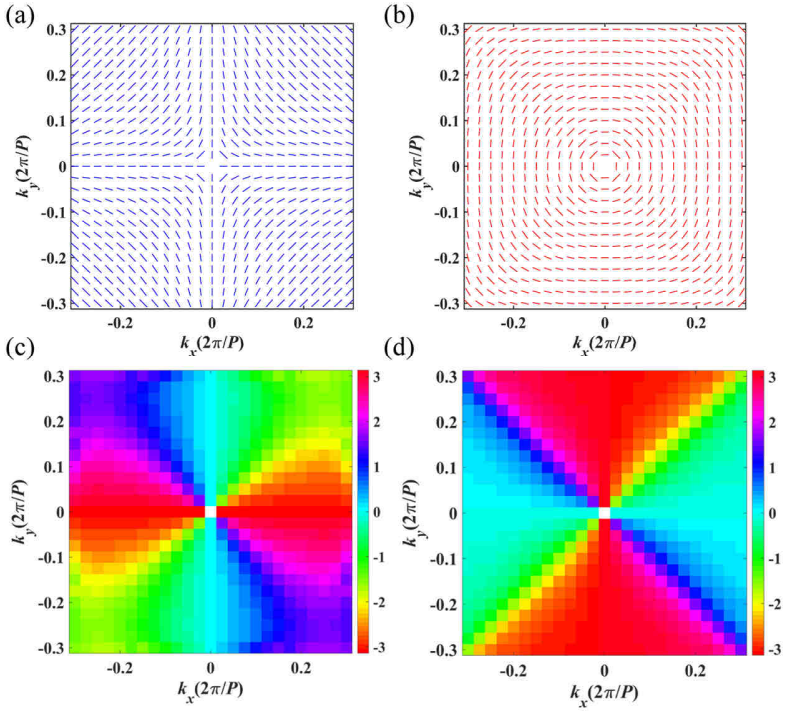

Fig. S4 (a-b) Far-field polarization maps of the qBIC and mBIC, respectively. (c-d) Azimuthal angle maps of the polarization for the qBIC and mBIC, respectively.

5. Potential experimental implementation

The proposed PhC slab design is scalable and can be implemented across a broad range of frequencies. For instance, in the visible regime, a free-standing PhC slab can be fabricated using electron beam lithography followed by reactive-ion etching, with band structure characterization performed via momentum-space imaging spectroscopy [4]. In the terahertz regime, the PhC slab can be realized using photolithography in combination with deep reactive-ion etching, and its band spectrum can be measured using fiber-based terahertz time-domain spectroscopy [5].

References

[1] Papasimakis N, Fedotov VA, Savinov V, Raybould TA, Zheludev NI. 2016 Nat. Mater. 15, 263–271.
[2] Sadrieva Z, Frizyuk K, Petrov M, Kivshar Y, Bogdanov A. 2019 Phys. Rev. B 100, 115303.
[3] Zhen B, Hsu CW, Lu L, Stone AD, Soljačić M. 2014 Phys. Rev. Lett. 113, 257401.
[4] Wang X, Wang J, Zhao X, Shi L, Zi J. 2022 ACS Photonics 10(7), 2316-2322.
[5] Wang W, Srivastava Y K, Tan T C, Wang Z, Singh R. 2023 Nat. Commun 14(1), 2811.